Minimizing feature width in atom optically fabricated chromium nanostructures

W. R. Anderson,* C. C. Bradley, J. J. McClelland,† and R. J. Celotta
Electron Physics Group, National Institute of Standards and Technology, Gaithersburg, Maryland 20899
(Received 20 August 1998)

We present a study of factors that influence the feature width of nanostructures formed by atom-optical direct-write lithography. In this process, chromium atoms travel through a standing-wave laser light field and are deposited on a surface. Due to the atom-light interaction, the atoms are focused onto the surface in the standing wave nodes, producing a pattern of parallel chromium lines with widths as small as 28 nm and a spatial period of 212.78 nm. We present calculations and measurements of feature widths representing an exploration of the effects of laser power and laser-substrate separation. Strong qualitative agreement is seen between calculations and the measurements, but the observed feature widths are uniformly larger than theoretical predictions. Experiments in which the total amount of chromium deposited is varied indicate that this difference can be attributed to chromium growth behavior. [S1050-2947(99)09503-7]

PACS number(s): 42.50.Gy, 03.75.Be, 66.10.Cb, 81.10.Bk

I. INTRODUCTION

Fabricating nanoscale structures by atom-optical manipulation of neutral atoms has recently been the subject of considerable study, due to a number of potential advantages presented by this technique. Neutral atoms from a thermal beam have small ($\sim$pm) de Broglie wavelengths and negligible long-range repulsive interactions, so resolution can, in principle, be very high. Also, this process is intrinsically direct write, so that resists and other chemical processing can be eliminated, making it easier to grow contaminant-free, structured films. Another advantage is that precise parallel patterning of large areas with nanoscale structures is readily attainable with the atomic manipulation methods developed to date.

A particular atom manipulation scheme that has been investigated in some detail utilizes the light forces exerted on an atom traveling through a near-resonant laser standing wave. When the standing wave is located sufficiently close and parallel to a surface, it has been shown that the light field can concentrate atoms into a periodic array of features with size well into the sub-100-nm regime (Fig. 1). This was first demonstrated with sodium [1], and subsequently with chromium in one [2,3] and two [4,5] dimensions, and also using aluminum [6].

In this paper, we present a detailed experimental and theoretical investigation of laser-focused atomic deposition of chromium in a one-dimensional standing wave. In order to probe the resolution limit of this process, we explore some of the experimental parameters that influence the nanostructure feature widths. Specifically, we examine how the measured widths vary with the standing wave (SW) intensity and its location relative to the substrate. Also, we study the effect of growth-related parameters, in particular, the total amount of deposited material and the substrate temperature. In conducting these studies we find that surface and growth-related phenomena have a significant effect on the deposited feature width. Hence they constitute an important aspect of the laser-focused atomic deposition process that has previously not been adequately addressed [7].

II. STANDING WAVE LENS FOR ATOMS

When an atom interacts with a near-resonant light field, the absorption and emission of photons causes a transfer of momentum and a corresponding change in the atomic motion. This motional change, which may be regarded as resulting from a sum of conservative and velocity-dependent, nonconservative forces, has proven very useful for manipulating atoms. For example, many implementations and applications of laser cooling and trapping have been demonstrated [8]. Such applications rely heavily on the nonconservative components of the force, which can be used to remove kinetic energy from an atomic vapor, cooling it to very low temperatures. The conservative component of the light force, on the other hand, is the most useful for focusing atoms on the nanoscale. This is because the nonconservative optical force involves spontaneous emission, which introduces a random component that can broaden feature sizes. Also, a conservative interaction allows the development of optical analogies for analyzing the trajectories of atoms.

The laser-atom interaction may be considered entirely conservative if the laser is tuned to a wavelength sufficiently far from any atomic resonance. Of course, to obtain a mechanical effect the laser is still kept sufficiently near a single resonance, so that the effect is not too weak. In this regime,

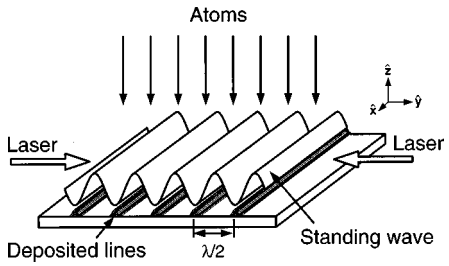

FIG. 1. Focusing of atoms in the nodes of a laser standing wave for deposition of nanoscale features on a substrate.

*Present address: Lighthouse Inc., Charlottesville, VA.
†Author to whom correspondence should be address. Electronic address: jabez@epg.nist.gov

and assuming there is only a single atomic transition near the laser frequency, the potential experienced by a two-level atom is given by the expression [9]

$$U=\frac{\hbar\Gamma^2}{8\Delta}\frac{I}{I_0}, \tag{1}$$

where Γ is the natural linewidth of the atomic resonance, Δ is the frequency detuning of the laser from the atomic resonance, I is the laser intensity, and I_0 is the saturation intensity associated with the atomic resonance [10]. We note that this interaction remains conservative only for times short compared with the spontaneous emission time $\tau_{sp} \sim (8\Delta^2/\Gamma^3)(I_0/I)$.

Considering the simple relationship between potential energy and light intensity displayed in Eq. (1), it is straightforward to see that a laser standing wave may be used to focus atoms on the nanoscale. If a laser beam propagating along $\hat{y}$ is retroreflected, the light intensity in the resulting standing wave has a spatial dependence given by $\sin^2(ky)$, where $k=2\pi/\lambda$ is the wave number of the laser light. As long as the atom-light interaction is conservative, atoms encountering this standing wave move on a potential energy surface that has a series of minima at integral multiples of $\lambda/2$. Near these minima, the potential is approximately proportional to k^2y^2. For an atom traveling along $\hat{z}$, that is, across the standing wave, such a transverse quadratic potential has precisely the dependence required for first-order (Gaussian) focusing. The result is that the field near each node of the standing wave acts as a lens with an effective aperture of a few hundred nanometers, capable of focusing atoms into an area a few nanometers in size.

The atom-optical properties of a laser standing wave have been examined in some detail using a classical trajectory approach [11,12]. Based on the quadratic dependence of the potential, the paraxial approximation can be used to derive a well-defined focal length for the lens formed in the standing wave node [13]. For a standing wave with a Gaussian envelope along $\hat{z}$, this focal length is given in the thin lens limit by [12]

$$f=\sqrt{\frac{2}{\pi}}\frac{1}{wk^2}\frac{E_0}{U_0}, \tag{2}$$

where w is the $1/e^2$ intensity radius of the Gaussian beam, E_0 is the kinetic energy of the atoms, and U_0 is the maximum potential energy modulation depth of the standing wave.

Equation (2) describes the behavior of a lens in the limit of weak focusing, i.e., when $f \gg w$. In the strong lens limit, allowance must be made for the possibility of immersion focusing, which occurs when the focal location is within the laser light intensity. Immersion focusing can be treated numerically for a Gaussian standing wave, or analytically for a laser with constant intensity along $\hat{z}$. In the latter case the location of the focus is given by [12]

$$z_f=\frac{\pi}{2k}\sqrt{\frac{E_0}{U_0}}, \tag{3}$$

where z_f is referenced from the point where the intensity is assumed to turn on instantaneously.

Considering Eqs. (2) or (3), a rather simple picture of the lens action as a function of laser intensity emerges. We see that, since $U_0 \propto I_0$, the focal location varies as I_0^{-1} for the thin lens case, or as $I_0^{-1/2}$ for the immersion case. This simple dependence can be used to examine the intensity dependence of the atom beam width at a given ''image plane'' location downstream of the standing wave, at least for a monoenergetic and perfectly parallel incident paraxial beam of atoms. For such a beam, a plot of the atom beam width versus laser intensity will go through a minimum at a specific intensity, corresponding to the lens being ''in focus.''

For thin-lens focusing, the beam width at the image plane is minimized at the optimum in focus intensity, and grows for intensities either smaller or larger than this value. However, for an immersion lens, the behavior is more complex. When the intensity is increased beyond the value required for simple focusing, the atoms cross the beam axis before reaching the image plane, and then continue to feel a central force. Thus they can refocus at a position further downstream. For very high intensities, the trajectories of the atoms can cross the axis of the lens many times before reaching the image plane. This results in a series of minima in a plot of atom beam width versus laser intensity, one for each value of intensity that causes paraxial atomic trajectories to cross the lens axis at the image plane.

While the behavior of a monoenergetic, parallel atom beam in the classical paraxial limit is useful for finding the location of a focus, it provides no information about the atom beam width at the focus. In order to make estimates of this it is generally necessary to go beyond the paraxial approximation. In addition, atom diffraction can become an important contributor to beam width.

Even in the paraxial limit, however, broadening of the focal width occurs when account is taken of atoms entering the lens with a range of velocities and angles relative to the axis. In a nominally in-focus lens, these atoms will miss the focal spot and hence cross the image plane off-axis, leading to an increased focal width.

Of particular interest is the behavior of these atoms in the over-focused immersion lens. In such a lens, the atoms will generally go through several crossovers, as previously discussed for the parallel, monoenergetic beam. If a range of velocities and angles is included, however, these crossovers will not be observable at the image plane because trajectories with different angles and velocities cross the axis at different locations. The result will be an overall concentration of atoms in the low intensity region of the node, more or less regardless of the exact velocity or incident angle. We refer to this behavior as ''channeling'' of the atoms in the standing wave node [14]. In this channeling regime, the insensitivity to velocity and angular spread in the beam is a great advantage. The beam widths, however, are not as small as attainable with true focusing, and they quickly degrade as the gap between the region of light intensity and the surface increases.

The interplay between true focusing and channeling, and also the degree to which the lens is thin or immersion, are central issues in discussing the behavior of laser-focused atomic deposition. Because a very fine focus is the main goal in such a process, it is advantageous to make the focal length of the lens as short as possible. Since much shorter focal

lengths can be achieved with an immersion lens, it is typical to get the laser beam as close to the surface as possible. Not only does this allow a finer focus, but it also enables the lens to be used in a channeling mode. Since in practice most experiments are done with thermal atom beams and imperfect collimations, this is a significant advantage. Furthermore, it is generally the case that the laser power required to get a focal length of the order of the laser beam size is fairly small (7.3 mW for Cr focusing in a Gaussian laser beam detuned by 500 MHz [12]). Hence, it is relatively easy to increase the laser power well into the channeling regime. It should be noted, though, that an immersion lens with light intensity all the way up to the substrate surface is generally not possible because of diffraction of the laser light by the edge of the substrate. Thus any laser lens will also have some component of thin lens behavior compounded with its other properties.

The atom-optical properties of a standing-wave lens can therefore be somewhat complex. General trends can be explained in terms of simple optical concepts in some limiting cases, but often there are a number of phenomena present, and the behavior is more subtle. To elucidate some of the behavior of such a lens, we have studied the feature width of deposited structures both theoretically and experimentally as a function of two parameters: laser intensity and location of the standing wave above the surface.

III. CALCULATIONS

The goal of the calculations presented in this paper is to model as precisely as possible the experimental conditions present during the depositions described in the experimental section. By comparing the feature widths predicted by the model with the observed ones, we can verify our understanding of the basic processes of laser-focused atomic deposition.

Our basic approach to the modeling has been described in detail in Ref. [12]. In essence, a large number of classical trajectories through the lens are calculated for different initial conditions of position, velocity and angle. Each trajectory is assigned a probability based on a uniform spatial distribution, a thermal longitudinal velocity distribution (derived from the oven temperature) and a laser-cooled transverse velocity distribution. At the image plane, a histogram of probabilities is accumulated as a function of position, resulting in a predicted flux distribution at the surface.

For all results we describe, the oven temperature was taken to be 1800 K, a temperature that has an associated most-probable longitudinal velocity of 926 m/s [15]. The transverse velocity distribution was assumed to be Gaussian and uncorrelated with the longitudinal velocity distribution, as would be appropriate for completely equilibrated transverse laser cooling. The width of the transverse velocity distribution was derived from the full width at half-maximum of the angular distribution in the beam, as measured in a fluorescence experiment [16]. For each calculation, the measured value 0.17 mrad was used. In total 360 000 trajectories were traced, corresponding to 400 initial y positions, 30 initial velocities, and 30 initial angles.

To account for the fact that different magnetic sublevels in the chromium atom have different interaction strengths with the laser light, and the fact that there will in general be a distribution in sublevel populations, additional averaging was carried out. In the depositions described here the standing wave laser beam was linearly polarized at an angle of 45° relative to the substrate surface (this angle was chosen for experimental convenience). An easy (but approximate) way to treat the sublevel averaging with this polarization configuration is to determine the magnetic sublevel populations in the basis set with quantization axis along the laser polarization, and then assign relative intensity strengths based on the squares of the Clebsch-Gordan coefficients for the associated $\Delta M=0$ transitions. These strengths are $\frac{1}{4}$ for the $M=\pm 3$ population, $\frac{3}{7}$ for the $M=\pm 2$ population, $\frac{15}{28}$ for the $M=\pm 1$ population, and $\frac{4}{7}$ for the $M=0$ population. To obtain the sublevel populations in this basis, we make an assumption about how the laser cooling leaves the population. In the basis with quantization axis along the laser propagation direction, we assume that $\frac{1}{3}$ of the population is in each of the $m=\pm 3$ states and $\frac{1}{6}$ of the population in each of the $m=\pm 2$ states. This distribution is arbitrarily chosen, yet it reflects the sublevel populations typically seen in polarization gradient cooling [17]. We then rotate the basis set into the direction of the laser polarization, and obtain populations of 0.0417 in each of the $M=\pm 3$ states, 0.1459 in each of the $M=\pm 2$ states, 0.2083 in each of the $M=\pm 1$ states, and 0.2083 in the $M=0$ state. We note that treatment of the sublevel populations in this way is a simplification, since it ignores all coherences between the states. Nevertheless, since so much averaging is carried out in the calculation, it is unlikely that any significant effects of coherences would survive. Furthermore, the concentration on populations of states rather than coherences is in keeping with the classical approach of the calculation. In addition, we note that we have ignored any possible mixing of magnetic sublevel populations induced by a residual magnetic field. In the experiment the earth's field is compensated by a set of Helmoltz coils to a level of $0\pm 2\ \mu$T, so any mixing is expected to be small and have minimal effects.

To trace classical trajectories through the standing wave lens the equation of motion based on a spatially dependent potential is solved. In the simplest scenario the potential given by Eq. (1) could be used for this purpose. However, putting in experimental values shows that the conditions of large detuning $[\Delta \gg \Gamma(I/2I_0)^{1/2}]$ and low excited state population, required for Eq. (1) to be valid, are not met in some cases. To do better in handling these situations, we are faced with either solving a much more complicated set of time-dependent optical Bloch equations [18], or approximating the potential with a steady-state average over ground- and excited-state populations [19]. Considering the fact that the atomic population approaches its equilibrium state with a time constant $\sim 1/\Gamma$, and that the average atom is exposed to the light field for a time about twice this long (as given by the laser beam radius divided by the average velocity), it is a reasonable approximation to use the equilibrium potential. In fact, because the light field has a Gaussian profile and hence turns on gradually, the atomic state population distribution is driven nearly adiabatically and is never far from its steady-state value [20]. We should note, however, that under these conditions there is a fair probability of spontaneously emitting a photon during passage through the standing wave lens. Nevertheless, one or two photon recoils have a negligible

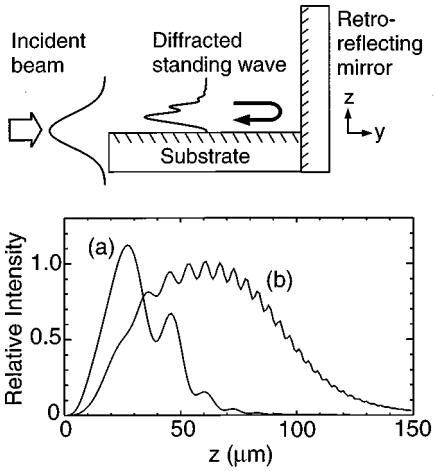

FIG. 2. Diffraction of a Gaussian standing-wave laser beam. Calculations are done assuming the incident beam has a 60-μm $1/e^2$ radius, and the substrate and retroreflecting mirror are perfectly reflecting. Profile (a) is calculated with the incident Gaussian beam center located at the substrate surface, and (b) is calculated with the center located 60 μm above the surface. The oscillations in the intensity are due to diffraction from the edge of the substrate.

effect on the trajectory of an atom traveling at thermal speeds over a distance of a laser beam radius, so the mechanical effects of spontaneous emission can be ignored.

Accordingly, the potential that the atoms travel on as they pass through the lens is taken to be [9,19]

$$U(x,y,z)=\frac{\hbar\Delta}{2}\ln\left[1+\frac{C_M I(x,y,z)}{I_0}\frac{\Gamma^2}{\Gamma^2+4\Delta^2}\right], \qquad (4)$$

where $I(x,y,z)$ is the spatially dependent intensity of the standing wave, C_M is the Clebsch-Gordan factor discussed above, $\Delta/2\pi$ is the experimentally set detuning of 500 MHz, $\Gamma/2\pi$ is the natural linewidth of Cr (5.0 MHz), and I_0 is the two-level saturation intensity for the $^7S_3\rightarrow{}^7P_4$ transition in Cr (85 W/m^2).

Because of the various roles played by channeling and thin-lens focusing in the standing-wave lens, care was exercised in modeling the laser intensity profile in the direction normal to the substrate—that is, along the z direction, or the direction of atomic flux. Since the nominal geometry for many laser-focused atomic deposition experiments has been to have a Gaussian laser beam bisected by the edge of the substrate, the z dependence of intensity has often been approximated by a half-Gaussian going up to the surface. On analysis of our experimental geometry, we have found that there is in fact a significant amount of diffraction of the Gaussian beam as it passes across the surface. To account for this we have numerically calculated an intensity distribution assuming a perfectly reflecting substrate surface and retroreflecting mirror. In this calculation the diffracted electric field of the incident laser beam was combined with the further-diffracted retroreflected beam at the point of deposition (1 mm from the substrate edge). The result is a standing-wave intensity profile that starts at zero at the substrate surface, grows over a distance of a few tens of micrometers, and then decays with a series of oscillations. Figure 2 shows intensity profiles calculated in this manner and used in the trajectory calculations. Two profiles are shown, corresponding to the two situations modeled—one with the incident Gaussian beam cut at its center by the substrate edge, and the other with the Gaussian beam cut one beam radius away from its center.

IV. EXPERIMENT

The laser-focused atomic deposition experiments presented here were conducted with chromium atoms as the deposited species. Chromium is a good material for these experiments for a number of reasons. From an atom-optical manipulation perspective it is relatively convenient, since (a) it is nearly mono-isotopic (84% naturally occurring as ^{52}Cr), (b) the dominant isotope lacks hyperfine structure (which can produce population traps during laser cooling), and (c) the principal atomic resonance transition ($^7S_3$-$^7P_3$) is at a readily accessible wavelength ($\lambda=425.55$ nm, in vacuum). Also, chromium is known to have good growth properties and forms a very thin ($\sim$1 nm) passivating oxide, allowing it to be conveniently stored and analyzed in air.

All depositions were carried out in an ion-pumped vacuum system with typical pressure 10^{-6} Pa (10^{-8} Torr) in the deposition region while depositions were in progress. A beam of atomic Cr was produced with a commercial, high-temperature cell. In the cell, a solid piece of Cr was held in a zirconia ceramic crucible with a 1 mm-diameter aperture and heated to 1800–1900 K. At a distance of 320 mm downstream from the atom source, the atomic beam was precollimated with a 1-mm-square aperture to a divergence of 6 mrad. After passing this aperture, the atoms entered a transverse laser cooling region, where they were further collimated before passing through the standing wave lens array located on the surface of the substrate. Substrates consisted of $3\times10\times0.4$-mm-thick polished Si[100], which had a native oxide layer, wiped clean with optical-grade acetone and methanol prior to their placement in vacuum.

A. Optical system

Figure 3(a) shows a schematic of the optical system used for carrying out the laser cooling and atom focusing in the experiment. Laser light was produced by a commercial ring dye laser pumped by a UV argon ion laser. With stilbene-3 laser dye pumped by 4 W of UV light, approximately 250 mW of light at 425 nm was available for the experiment. Using two beam splitters and an acousto-optic modulator (AOM), four beams were created from the original dye laser output. Two of these had a frequency 495 MHz above the atomic resonance, and two had frequency 5 MHz below resonance. These frequencies were set by tuning the laser 495 MHz above resonance, and downshifting by 500 MHz with the AOM. One of the beams tuned just below the atom resonance was used to provide transverse cooling/collimation of the atom beam, and the other was used for locking the output frequency of the laser (see below). The laser beams detuned 495 MHz above resonance (one of which was the unshifted beam out of the AOM) were used to form the SW near the substrate, and to provide active locking of the separation between the substrate and the retroreflecting mirror (discussed in more detail below).

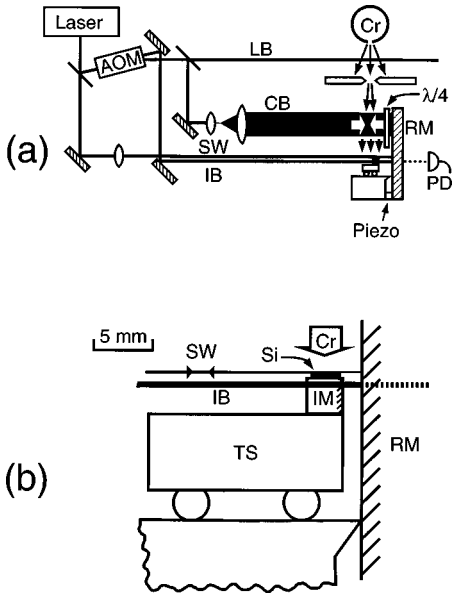

FIG. 3. (a) Essential components of the experiment. The dye laser output, tuned 495 MHz above the atomic resonance, is split into two components, one of which provides the laser SW beam. The other beam is redshifted 500 MHz by an AOM and further split to provide a locking beam (LB) that is used to eliminate laser frequency drift, an interferometer beam (IB) for interferometric stabilization of the sample/mirror spacing, and a cooling beam (CB) for transverse laser cooling/collimation of the atom beam. Interferometer fringes are detected with a photodiode (PD) and used in a feedback loop to rotate the RM about a knife edge by the action of a piezoelectric transducer. (b) Detailed view of the sample stage. The temperature-controlled stage (TS) is thermally isolated from the glass ceramic knife edge with glass balls. The RM hinges at the knife-edge with the pivoting motion controlled by the piezoelectric transducer [see (a)]. The silicon substrate (Si) sits on top of the IM, which has a dielectric coating on the side nearest the retroreflecting mirror. The collimated Cr beam is aligned parallel to the RM within 1 mrad and strikes the substrate normally after traveling through the SW.

The dye laser wavelength was stabilized against long-term drift via a signal derived from atom beam fluorescence excited by a locking laser beam. The fluorescence from the intersection of the locking beam and an uncollimated region of the atomic beam was imaged onto a split photodiode [21]. Any drift in the laser frequency caused the region of fluorescence to move along the laser beam propagation direction. This motion caused a difference signal to be produced by the split photodiode, which was fed back to the dye laser external scan input.

The transverse cooling region, which was located a distance of 350 mm from the Cr source, consisted of a linearly polarized laser beam that crossed the atom beam at right angles. After crossing the atom beam, this laser light passed through a quarter-wave retarding plate and was retroreflected, creating a region of transverse one-dimensional polarization-gradient cooling [22]. The 20-mW (single-beam, incident power) cooling beam was nearly Gaussian and approximately 2×15 mm ($1/e^2$ intensity full width) in cross section.

The standing wave was formed from 20 mW of the output of the dye laser. The light was focused to a beam waist at the retroreflecting mirror (RM) in the vacuum chamber. The SW beam waist was profiled with a scanning-slit detector and the result agreed well with a Gaussian profile with $1/e^2$ radius $w_0 = 60 \pm 5$ μm.

B. Sample holder

Figure 3(b) shows a scale drawing of the sample holder, which was designed to provide (a) motion of the sample-mirror assembly for alignment and positioning in or out of the atom beam, (b) registration of the sample with respect to the standing wave (or equivalently, the retroreflecting mirror), and (c) controlled variation of the substrate temperature.

Motion of the assembly was provided by mounting it on a commercial translation/rotation vacuum feed-through manipulator. All degrees of motion were possible, including x, y, and z translation, as well as tilt and rotation.

Registration of the substrate surface with the SW light field involved ensuring both that the SW nodes did not drift relative to the sample, and also that the surface was parallel to the light propagation direction. The first of these requirements was achieved by active control of the RM-sample separation. For this purpose the sample was clamped on the side of a mirror [the interferometer mirror (IM)], which had reflectance 56% at 425 nm. The IM, together with the RM, formed a Fabry-Perot interferometer with 1 mm spacing. Passing a laser beam derived from the frequency-locked dye laser through this interferometer provided a measure of the RM-sample separation. To keep this separation constant the RM was pivoted about a knife edge on the sample mount with a piezoelectric transducer, and the bias voltage on this transducer was adjusted to maintain maximum interferometer transmission as monitored by a photodiode. To facilitate this, a 100-Hz oscillating voltage was added to the bias to introduce a 1-nm dither in the mirror spacing. The photodiode output was detected by a lock-in amplifier and the resultant derivative signal was fed back to the transducer. Parallelism of the substrate surface with the SW propagation direction was ensured by precisely grinding the sides of the IM (on which the substrate rested) to be perpendicular to its reflective mirror face with an accuracy 0.5 mrad. Alignment of the Fabry-Perot interferometer therefore ensured that the sample was perpendicular to the RM, and hence parallel to the SW propagation.

To control the sample temperature, the sample and IM were held in thermal contact with a molybdenum platform, which was part of a temperature-controlled stage. The molybdenum platform was heated by a tungsten heater wire and cooled via conduction through a copper braid and 19-mm-diam copper vacuum feed-through in thermal contact with a liquid nitrogen reservoir located outside the vacuum chamber. The electrical current sent through the heater wire was controlled with a feedback system that held the substrate at a fixed temperature, as monitored by a thermistor mounted onto the substrate with thermally conductive vacuum-compatible epoxy. The stage was thermally insulated from the rest of the mount by four 3-mm-diam glass balls. These balls rested on a slab of low thermal expansion glass-ceramic, which provided the knife-edge pivot for the RM.

C. Deposition and sample analysis

Before conducting a deposition, the collimation of the atom beam as produced by the one-dimensional polarization

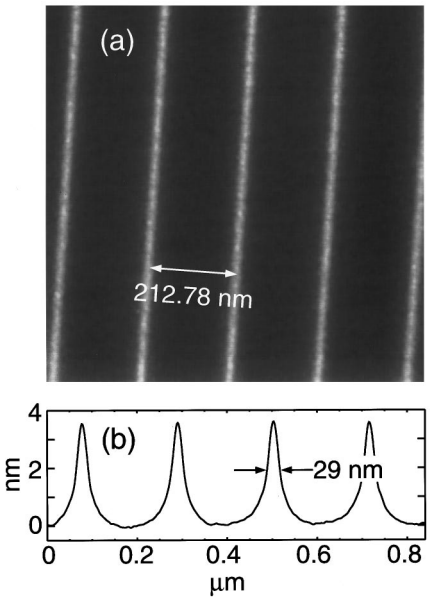

FIG. 4. (a) 1×1 μm AFM image of chromium lines formed by laser-focused atomic deposition. (b) A line scan taken from (a), where averaging has been carried out over a distance of 400 nm along the lines. The average FWHM of the four peaks in (b) is 30 nm and the peak-to-valley height is 3.6 nm. Accounting for AFM tip effects in this case reduces the measured Cr feature width to 29 nm (see text).

gradient laser cooling was measured and optimized. For this purpose the entire sample mount was moved out of the path of the atom beam along the direction of SW propagation ($\hat{y}$ direction), and the alignment was adjusted by tilting and rotating the sample manipulator. As described in Ref. [22] the collimation was checked by inserting a knife-edge into the atom beam and imaging laser-induced fluorescence after a free-flight distance of 800 mm. Using this method the angular width of the beam was determined to be in the range 0.17–0.2 mrad (full width at half-maximum (FWHM)) for all depositions.

After optimizing the collimation, the atom beam was blocked and the sample mount was translated back into position without disturbing the alignment of the RM. The IM-RM separation was locked with the interferometer system, and then the atom beam block was removed for a fixed deposition time. In many cases multiple depositions were carried out on a single silicon sample by translating the substrate in a direction perpendicular to both the atom beam and the SW (that is, in the x direction). When all depositions were completed the vacuum system was vented with dry nitrogen and the sample was removed for analysis with an atomic force microscope (AFM).

A sample AFM image showing the surface topography of a 1×1 μm area of a deposition is shown in Fig. 4(a). Figure 4(b) shows an averaged linescan, as used to perform measurements on the surface topography. Averaging of the linescans was carried out along the Cr lines over a distance of approximately 400 nm. For width measurements, the full widths at half-maximum of all peaks in the linescan were measured and averaged. The Cr features on the sample shown in Fig. 4 have an average FWHM of 29 nm (corrected for AFM tip width as described below), and a peak-to-valley height of 4 nm. All lateral measurements taken from the AFM were calibrated with the pitch of the chromium lines, which is assumed to be 212.78 nm. This pitch is believed to be accurate to at least 0.01%, since it is set by the wavelength of the laser, whose frequency is referenced to an atomic transition.

In addition to measuring the topography of the surface, we also determined the total amount of Cr deposited. This was done by protecting part of the Cr film, chemically etching the unprotected part of the film with commercial Cr etchant [23], and measuring the height of the resulting step edge with the AFM. This method gives a good measure of chromium thickness because the etchant removes all the chromium, yet etches the silicon substrate by less than 0.2 nm under our conditions. On each sample, the average thickness was obtained by measuring an etched edge far from where the SW passed, in a location where the chromium formed a uniform layer.

By etching in the region covered by the SW, we were also able to measure the amount of material in the valleys, or regions between the Cr lines. Typical substrate-to-valley heights were 1.4 nm on a deposition that had a 3-nm peak-to-valley height, and 7 nm for a deposition with 47-nm peak-to-valley height.

In obtaining measurements from the AFM images, care was taken to account for distortions due to finite AFM tip size. An AFM image provides an exact representation of surface topography only if the tip is sharper than any features on the actual surface. In general, since AFM tips are not arbitrarily sharp, actual AFM images also reflect the shape of the tip. For the measurements presented here, the feature widths were generally larger than the AFM tip used, so tip-produced width broadening is not very significant [24]. Nevertheless, it is not completely negligible and we have accounted for it as follows. We used an algorithm developed by Villarubia [25] to erode an AFM tip model from raw AFM images. To obtain a tip model, we imaged a sharp artifact consisting of a silicon grating structure with triangular shape and nominal peak radius of less than 10 nm. While this artifact is quite sharp, its size is not completely negligible compared with the tip, and there remains some degree of uncertainty as to its exact shape. Thus the resulting tip model is an overestimate of the tip shape and width. Eroding our data with this model therefore introduces uncertainties and also leads to systematic underestimation of feature widths. Because uneroded data results in possible overestimation of feature width, and eroded data results in possible underestimation, we have chosen to present width measurements that are an average of the raw and eroded widths, and have indicated the range from eroded to raw values with error bars. As examples of the effects of erosion, we note that Cr features with 4-nm peak-to-valley height eroded from 29 to 27 nm FWHM, and features with 16-nm peak-to-valley height eroded from 63 to 58 nm FWHM.

V. RESULTS AND DISCUSSION

To examine the role played by laser intensity, and hence potential depth, in focusing atoms, we present a series of measurements as a function of laser intensity. Experimentally, the intensity that the atoms experience can be altered

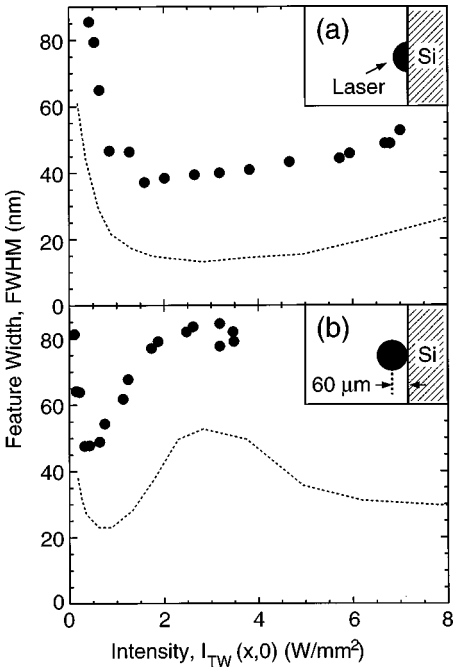

FIG. 5. Feature width as a function of laser intensity for the case when (a) the center of the incident Gaussian laser profile intercepts the substrate surface and (b) when the center of the incident Gaussian laser beam is separated from the substrate surface by one beam waist (60 μm). The laser configuration is graphically represented by the inset diagrams. The dotted lines are the results of the numerical ray-tracing model evaluated at several intensities for each case. The plotted data are the averages of the measured and eroded widths. For these data the differences between the measured and eroded widths are typically 2–3 nm, or about the size of the plotted symbols for this data.

by changing the overall intensity of the SW laser beam. Alternatively, the same information can be obtained by looking at different regions on the substrate, since the intensity varies across the laser beam. We have made use of the Gaussian profile of the laser and obtained a series of AFM images at different values of x along the substrate. To correlate the x positions with SW intensity, we have plotted the FWHM of the features versus the incident traveling wave (TW) intensity $I_{\mathrm{TW}}(x,0)$ at the substrate just before diffraction takes place. This quantity is obtained by setting $z=0$ in the expression for the TW intensity

$$I_{\mathrm{TW}}(x,z)=\frac{2P_0}{\pi w^2}\exp\left(\frac{-2}{w^2}(x^2+z^2)\right), \tag{5}$$

where w is the measured $1/e^2$ radius and P_0 is the measured total incident laser power. While the actual SW intensity at a given position on the substrate is modified by diffraction and addition of the retroreflected beam (see Fig. 2), it is nevertheless proportional to $I_{\mathrm{TW}}(x,0)$. Thus this quantity provides a convenient parameter for comparison of experiment and calculation.

In Fig. 5(a) we show the intensity dependence of the feature width [26] for the case where the incident TW is positioned such that half the retroreflected power is blocked by the substrate (schematically depicted by the figure inset). As the intensity increases from zero, Fig. 5(a) shows a decrease in the feature width up to an intensity of about 2 W/mm^2 [27], after which there is a gradual increase. The low-intensity decrease can be interpreted as a bringing of the atom lens into focus for the most probable velocity in the atom beam. The feature width reaches a minimum at an intensity that puts the focal spot of the lens at the substrate. Based on this model, we might expect a rapid rise in the width as the intensity is further increased and the focal location moves away from the substrate surface. Instead, the data show only a slow rise in the feature size. This is due to the effects of channeling, which tends to keep the atoms concentrated as the laser intensity is increased.

Shown by the dotted line in this figure is the result of numerical modeling, as discussed in Sec. 3. The experimentally measured laser power P_0 and beam radius w were used in the model and no parameters were freely adjusted. The trend is in excellent agreement with the data. The difference in magnitude between the model and the data is an important issue and will be discussed later.

The data shown in Fig. 5(b) were taken in the same manner as the data in Fig. 5(a) except that the standing wave was shifted away from the substrate by one $1/e^2$ beam radius (60 μm) in the $\hat{z}$ direction. As in Fig. 5(a), there is excellent agreement between the shape of the experimental data and the numerical ray tracing calculation. Here the width exhibits a sharp minimum near 0.5 W/mm^2, followed by an increase for higher intensities and an apparent peak near 3 W/mm^2. The minimum occurs at lower intensity than in Fig. 5(a), and this can be explained by noting that since the substrate is further from the standing wave, minimum feature width requires a longer focal length, which is obtained at lower intensities. As in Fig. 5(a), channeling plays a significant role in the formation of the features, causing the width to level off with intensity. In this case, though, it is less effective since there is less power near the substrate. The depositions used for Figs. 5(a) and 5(b) were both of 5 min duration and had an average Cr thickness of 4 nm.

Overall, the magnitudes of the feature sizes in both Figs. 5(a) and 5(b) are larger than predicted in the calculations by 20–30 nm. To explore the source of this discrepancy, we must consider the following possibilities: (1) we have not accurately represented the experimental conditions in the calculations; (2) there are additional atom-optical effects not taken into account in the calculations; or (3) the final, observed distribution of Cr atoms does not reflect the actual flux distribution upon deposition—that is, there is redistribution through surface diffusion and/or growth in preferential directions.

To eliminate the first of these possibilities, we have carefully measured the SW laser power and intensity distribution, and also modeled the diffraction of the laser from the substrate edge, as discussed above. We have also verified the assumed Maxwell-Boltzmann distribution in the longitudinal velocities of the atom beam, and measured the collimation of the atom beam as produced by the transverse laser cooling. As there are some assumptions that go into deriving the transverse velocity spread from the observed angular width of the atom beam, we have taken the additional experimental step of varying the amount of collimation and observing the

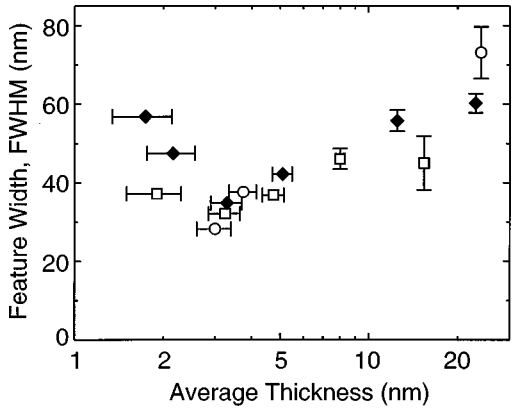

FIG. 6. Feature width as a function of Cr thickness. The width of features (average FWHM as discussed in the text) is plotted as a function of average Cr thickness, as determined by the etching procedure described in the text (note the logarithmic scale of the ordinate). The thickness uncertainty (± 0.4 nm), represented by horizontal error bars, stems from our inability to ensure that the etch procedure removes material precisely to the Cr/Si interface. The widths of the averaged line scans are plotted with the vertical error bars spanning the range between the as-measured and AFM-tip eroded widths. Symbols differentiate data taken on separate runs.

feature width of the deposited lines. No variation of the feature width was seen over a range of collimations from 0.16 to 0.37 mrad.

The second possibility is somewhat more problematical to eliminate. The calculations are inherently classical and hence do not take into account spontaneous emission, diffraction of the atoms, or dressed-state, multilevel phenomena associated with the true quantum mechanical nature of the laser-atom interaction. We have investigated diffraction by considering the distribution of impact angles found in trajectories that make up the central peak in the calculated flux distribution. By an uncertainty principle argument, this can be associated with a diffraction-limited spot size, which in the case of the calculations presented here is of the order 3 nm—an amount negligible compared with the actual results. Spontaneous emission and the other quantum mechanical phenomena cannot be completely eliminated; however, since the observed width broadening is independent of laser intensity, it is unlikely that these effects are significant.

The most likely explanation for the discrepancy between the calculations and the experiment lies in the behavior of the chromium during and after deposition on the surface. To study this further we looked at the dependence of the feature width on the amount of Cr deposited, which we varied by making samples with different deposition durations. If no changes occur in the chromium distribution during or after deposition, we would expect the feature width to be independent of the amount of chromium deposited. However, we have found a marked dependence on total chromium deposited.

In Fig. 6, the measured feature width is plotted as a function of average chromium thickness with the various symbols representing data taken in separate but nominally equivalent runs. We see that as a function of thickness, the width has a value near 55 nm at very low thickness, then decreases, going through a minimum near 3 nm thickness. After the minimum, the width rises steadily to a value of 70 nm at 24 nm thickness. The absolute minimum FWHM observed is 28 ± 1 nm for an average Cr thickness of 3 ± 0.4 nm thickness. The variation in linewidth is quite surprising, considering the near refractory nature of chromium and the fact that the depositions were conducted at room temperature. A possible explanation for the decreasing feature width at low coverage is that a higher mobility of Cr on the substrate material is slowly being replaced by a lower mobility of Cr on the Cr surface. The increase in width from the minimum can perhaps be attributed to an increase in chromium grain size with chromium thickness, once a significant amount of Cr is built up on the surface. Such an increase in grain size with chromium film thickness has been observed in other studies [28].

It is conceivable that the observed width increase above 3 nm Cr thickness might be due to drift of the sample relative to the laser standing wave, since the thicker depositions were made with longer deposition durations. However, since this type of drift typically gives rise to asymmetric features, which are not observed in the data, it is an unlikely explanation.

To further clarify the role of growth, we also examined the behavior of the width of features on samples where a uniform layer of chromium was applied directly over the Cr nanostructured film immediately after the laser-focused deposition. If the chromium atoms simply stayed where they landed, one would expect the surface to become rougher due to the random nature of deposition, but otherwise remain unchanged by the overlayer. On the other hand, with redistribution of the atoms, a change in shape of the Cr features would be observable.

To perform this experiment, two laser-focused depositions were modified by depositing a uniform layer of chromium (overlayer) on top of the patterned depositions (base layer). The two patterned base layers were deposited for different durations, yielding different initial profiles. One deposition contained features with nominal dimensions of 30-nm-wide by 4-nm-high (peak to valley). The features on the other deposition were nominally 65 nm wide by 35 nm high. The sample was then translated to a new position so that half of the base layer for each deposition was exposed to the atom flux from the oven. The standing wave laser was blocked while a uniform layer of chromium ($\sim$20 nm) was deposited. Due to the geometry of a physical aperture and the atom beam divergence, the overlayer thickness varies from 0 to 20 nm over a transition region $\sim$150 μm wide. By taking a series of AFM images while stepping through the transition region, we were able to measure the feature width dependence on overlayer thickness.

The data is presented in Fig. 7 as the broadening (increase in the FWHM) of the features versus overlayer thickness. Both samples, each with different base layer features but identical overlayers are shown in the figure differentiated by plot symbol. For each sample, we see an increase in the broadening from 0 to 10 nm as chromium is added to the overlayer, up to a thickness of 20 nm. Remarkably, the broadening is the same in each case even though the initial feature shapes were quite different. This provides additional evidence that Cr growth plays an important role in the observed broadening of laser-focused chromium depositions. It is possible that such growth could be explained by invoking

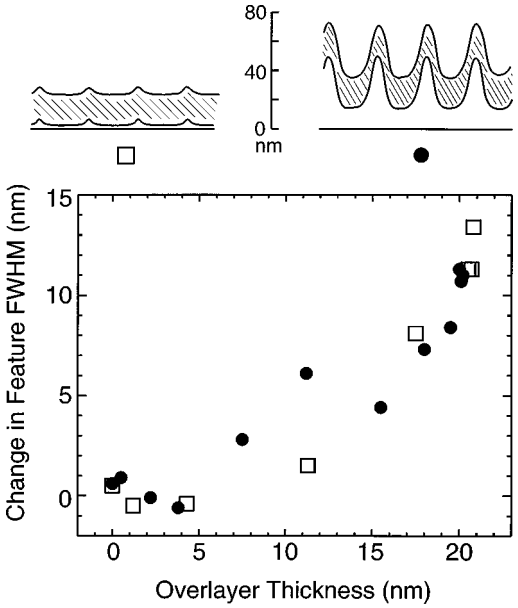

FIG. 7. Feature width as a function of Cr overlayer thickness. The open squares show the broadening that resulted when the base layer consisted of chromium lines measuring 30 nm FWHM by 4-nm peak-to-valley height. The filled circles give the broadening found when the the base layer had lines measuring 65-nm FWHM by 35 nm high. The diagrams above the plot are AFM line scans of the base layers and overlayers for each case, where the vertical placement of the line scans relative to the substrate has been determined via the etching procedure.

processes involving grain formation, which might be governed by differing rates for diffusion up versus down an atomic step edge [29].

We also examined the dependence of the feature size on the temperature of the substrate during deposition. Considering that we have seen significant effects due to redistribution of the chromium atoms in the surface, one might expect that there would be a temperature dependence to the observed feature widths. However, performing depositions at a number of substrate temperatures ranging from $-70°$ to $+90\,°C$ we saw no measurable change in the features. While this is perhaps surprising, it does not contradict the conclusion about the importance of growth issues. The mobility of chromium during growth is a complex phenomenon, governed by many processes with different activation thresholds. Energy for diffusion is not only available thermally, but also from the kinetic energy of the depositing atoms and their heat of fusion upon binding chemically to the surface.

In summary, we see excellent agreement between trends in the trajectory calculations and measurements for the feature size dependence on atom-optical parameters. We have seen a difference in absolute feature width comparing model to data, and we have shown that the difference depends on the amount of chromium deposited (either focused or deposited uniformly). We have strong evidence that details of chromium film growth phenomena are responsible for this observation.

Regarding the understanding of laser-focused atomic deposition, we have demonstrated that sub-30-nm (FWHM) features are possible in chromium with this nanofabrication technique, and we have reached a qualitative understanding of the focusing/channeling mechanism. Moreover, we have demonstrated that the further reduction of the feature size will benefit from careful studies of growth phenomena using well-characterized surfaces and controlled deposition conditions.

ACKNOWLEDGMENTS

The authors wish to thank J. S. Villarubia for discussions on scanning probe microscopy tip issues and for providing the numerical erosion software. We would also like to thank members of the Electron Physics Group, in particular, Mark D. Stiles, for useful conversations. This work was supported by the Office of Technology Administration of the U.S. Department of Commerce.

[1] G. Timp, R. E. Behringer, D. M. Tennant, J. E. Cunningham, M. Prentiss, and K. K. Berggren, Phys. Rev. Lett. **69**, 1636 (1992).

[2] J. J. McClelland, R. E. Scholten, E. C. Palm, and R. J. Celotta, Science **262**, 877 (1993).

[3] U. Drodofsky, J. Stuhler, B. Brezger, Th. Schulze, M. Drewsen, T. Pfau, and J. Mlynek, Microelectron. Eng. **35**, 285 (1997).

[4] R. Gupta, J. J. McClelland, Z. J. Jabbour, and R. J. Celotta, Appl. Phys. Lett. **67**, 1378 (1995).

[5] U. Drodofsky, J. Stuhler, Th. Schulze, M. Drewsen, B. Brezger, T. Pfau, and J. Mlynek, Appl. Phys. B: Photophys. Laser Chem. **65**, 755 (1997).

[6] R. W. McGowan, D. M. Giltner, and Siu Au Lee, Opt. Lett. **20**, 2535 (1995).

[7] Similar studies have been carried out for laser-focused sodium deposition; however, those results are not directly comparable to the present studies using chromium. See R. E. Behringer, V. Natarajan, and G. Timp, Opt. Lett. **22**, 114 (1997) and R. E. Behringer, V. Natarajan, and G. Timp, Appl. Surf. Sci. **104/105**, 291 (1996).

[8] See, e.g., J. Opt. Soc. Am. B **2** (1985), special issue on the mechanical effects of light, edited by P. Meystre and S. Stenholm; *ibid.* **6** (1989), special issue on laser cooling and trapping of atoms, edited by S. Chu and C. Wieman; C. N. Cohen-Tannoudji and W. D. Phillips, Phys. Today **43** (10), 33 (1990).

[9] J. P. Gordon and A. Ashkin, Phys. Rev. A **21**, 1606 (1980).

[10] We use the definition for saturation intensity that results in $\frac{1}{4}$ the population of a two-level system in the excited state, i.e., $I_0=\pi hc\Gamma/(3\lambda^3)$. See R. Loudon, *The Quantum Theory of Light* (Clarendon Press, Oxford, 1973), p. 28.

[11] K. K. Berggren, M. Prentiss, G. L. Timp, and R. E. Behringer, J. Opt. Soc. Am. B **11**, 1166 (1991).

[12] J. J. McClelland, J. Opt. Soc. Am. B **12**, 1761 (1995).

[13] The paraxial approximation applies when trajectories have small angles and travel close to the axis, i.e., when $dy/dz \ll 1$ and $ky \ll 1$.

[14] Yu. B. Ovchinnikov and V. S. Letokhov, Comments At. Mol. Phys. **27**, 185 (1992).

[15] In the experiments the temperature of the oven was different for different runs, ranging from 1800 to 1900 K, with an uncertainty of approximately 50 K. This amount of deviation has only a very minor effect on the outcome of the calculations.

[16] As discussed in Ref. [12] the flux probability as a function of longitudinal velocity v and angle α is given by

$$P(v,\alpha)\propto v^4 \exp\left[-\frac{mv^2}{2k_BT}\left(1+\frac{\alpha^2}{\alpha_0^2}\right)\right],$$

where m is the atomic mass, k_B is Boltzmann's constant, T is the oven temperature, and α_0 is related to the transverse velocity width resulting from laser cooling. The quantity α_0 can be obtained from a measurement of the full width at half-maximum α_{FWHM} of the angular distribution through

$$\alpha_0=\frac{\alpha_{\mathrm{FWHM}}}{2\sqrt{\sqrt{2}-1}}.$$

This relation is derived as follows. We assume α_{FWHM} is obtained from a fluorescence measurement, which means that it is representative of an angular distribution obtained by integrating the quantity $P(v,\alpha)/v$ over velocity. $P(v,\alpha)$ is divided by v in this case because $P(v,\alpha)$ alone is a flux distribution, and fluorescence measurements are sensitive to density. The resulting angular distribution is given by

$$F(\alpha)\propto\left(1+\frac{\alpha^2}{\alpha_0^2}\right)^{-2},$$

from which the expression for the full-width at half maximum is derived.

[17] P. Marte, R. Dum, R. Taïeb, P. D. Lett, and P. Zoller, Phys. Rev. Lett. **71**, 1335 (1993).

[18] See, e.g., L. Allen and J. H. Eberly, *Optical Resonance and Two-level Atoms* (Dover, New York, 1987).

[19] J. Dalibard and C. Cohen-Tannoudji, J. Opt. Soc. Am. B **6**, 2023 (1989).

[20] This has been verified by model calculations based on a two-level atom.

[21] J. J. McClelland and M. H. Kelley, Phys. Rev. A **31**, 3704 (1985); W. Jitschin, Appl. Phys. B: Photophys. Laser Chem. **33**, 7 (1984).

[22] R. E. Scholten, R. Gupta, J. J. McClelland, R. J. Celotta, M. S. Levenson, and M. G. Vangel, Phys. Rev. A **55**, 1331 (1997).

[23] A protective layer of PMMA (KTI Chemicals, Inc. 950K) was painted on the area of Cr that was not to be etched and cured at 100 °C for 1 h. The sample was then dipped in a Cr etchant (Cyantek CR-7) for 60 s at 25 °C and rinsed with distilled water. This left a step edge that had a transition width (10–90 %) of 15 nm. N.B. certain commercial materials are identified in order to adequately specify the experimental procedure. Such identification does not imply recommendation or endorsement by the National Institute of Standards and Technology, nor does it imply that the materials identified are necessarily the best for the purpose.

[24] The AFM tips used were commercially available etched silicon tapping-mode tips with nominal specifications 35° cone angle and 10 nm radius. On examining these tips with our artifact, we observed a noteworthy behavior. Under our scan conditions on the Cr samples, the tips became slightly dulled after about 10 min of scanning, reaching a steady-state shape with 25 nm radius and 50° cone angle. This dulling behavior was quite reproducible with a number of tips examined, and the shape appeared to be quite constant after the initial dulling period. We used this dulled shape as our tip model for eroding the data.

[25] J. S. Vilarubia, J. Res. Natl. Inst. Stand. Technol. **102**, 425 (1997).

[26] In all of the presented data there is an uncertainty in the quoted widths due to statistical variation of the deposited lines. As discussed in the text, we take a line average and then average four peaks in each AFM image. The peaks that are averaged have a typical feature width variation of 5–10 %. In addition we do not sample the entire $\sim 10^5$-μm^2 area of each deposition, but take a series of 1-μm^2 images which are taken to be representative of the sample.

[27] Intensity values presented in this paper have an associated uncertainty of approximately 10%, resulting predominantly from uncertainty in the measurement of laser power.

[28] D. Goyal, A. H. King, and J. C. Bilello, in *Electronic Packaging Material Science III*, edited by R. Jaccodine, K. A. Jackson, and R. C. Sundahl, MRS Symposia Proceedings No. 108 (Materials Research Society, Pittsburgh, 1988), p. 395.

[29] J. Villain, J. Phys. I **1**, 19 (1991); I. Elkinani and J. Villain, *ibid.* **4**, 949 (1994).